RESEARCH ARTICLE | MAY 02 2023

Eulerian–Lagrangian modeling of phase transition for application to cavitation-driven chemical processes

Special Collection: Cavitation

Francesco Duronio ; Andrea Di Mascio ; Angelo De Vita ; Valentina Innocenzi ; Marina Prisciandaro

Physics of Fluids 35, 053305 (2023)
https://doi.org/10.1063/5.0145568

Physics of Fluids ARTICLE scitation.org/journal/phf

Eulerian–Lagrangian modeling of phase transition for application to cavitation-driven chemical processes

Cite as: Phys. Fluids **35**, 053305 (2023); doi: 10.1063/5.0145568
Submitted: 6 February 2023 · Accepted: 12 April 2023 ·
Published Online: 2 May 2023

Francesco Duronio, Andrea Di Mascio, Angelo De Vita,[a] Valentina Innocenzi,[b] and Marina Prisciandaro

AFFILIATIONS

Department of Industrial and Information Engineering and Economics, Università degli studi dell'Aquila-Piazzale Ernesto Pontieri, Monteluco di Roio, 67100 L'Aquila (AQ), Italy

Note: This paper is part of the special topic, Cavitation.
[a]**Also at:** Consiglio Nazionale delle Ricerche, Istituto di Scienze e Tecnologie per l'Energia e la Mobilità Sostenibili (STEMS), Via G. Marconi 4, 80125 Napoli, Italy.
[b]**Author to whom correspondence should be addressed:** valentina.innocenzi1@univaq.it

ABSTRACT

Hydrodynamic cavitation is a promising technology for several applications, like disinfection, sludge treatment, biodiesel production, degradation of organic emerging pollutants as pharmaceutical, and dye degradation. Due to local saturation conditions, cavitating liquid exhibits generation, growth, and subsequent collapse of vapor-filled cavities. The cavities' collapse brings very high pressure and temperature; this last aspect is essential in some chemical processes because it induces the decomposition of water molecules into species with a high oxidation potential, which can react with organic substances. Properly exploiting this process requires a highly accurate prediction of pressure peak values. To this purpose, we implemented a multiphase Eulerian–Lagrangian code to solve the fluid-dynamic problem, coupled with the Rayleigh–Plesset equation, to capture the evolution of bubbles with the required accuracy. The algorithm was validated against experimental data acquired with optical techniques for different cavitation-shedding mechanisms. Then, we used the developed tool to investigate the decoloration of organic substances from a cavitation Venturi tube operating at different pressure. We compared the obtained results with the experimental observation to assess the reliability of the developed code as a predictive tool for cavitation and the possibility of using the code itself to assess scale-up criteria for possible industrial applications.

I. INTRODUCTION

Cavitation occurs in flow regions where the pressures drop below the vapor pressure. Vapor cavities develop as large voids or as clouds of bubbles and can be attached to a wall or travel in the mainstream flow. Experimental observations show that, depending on the flow conditions, two mechanisms lead to cavitation with bulk vapor shedding.[1] The first is a reentrant jet, typically when the attached or partial vapor cavity is short. The reentrant jet has the topology of a thin liquid film wedged between the solid boundary and the vapor cavity. It is periodically generated at the cavity closure region when the vapor cavity has reached its maximum length during a shedding cycle.[2] It then travels upstream until it causes cavity detachment. This detached cloud travels downstream and collapses where pressure has returned to a value higher than the vapor pressure. At the same time, a new vapor cavity begins to form. Figure 1 is a schematic view of the vapor cavity and the reentrant flow corresponding to the mid-plane in a cavitating Venturi tube. The second mechanism is condensation or bubbly shock and typically occurs when the operating conditions permit the attached vapor region to extend further downstream. This phenomenon relates to pressure waves propagating upstream and originated by the collapse of previously shed vapor.[3] Once these waves return at the attached vapor's rear edge, they trigger condensation shock fronts, causing vapor separation from the wall and cloud collapse. Detailed investigations about this mechanism on wedges and other geometries are in Refs. 4–6.

In both mechanisms, cavitation generates extreme conditions useful in specific chemical processes. In recent years, research activities aimed at the exploitation of the phenomenon of cavitation for biodiesel production,[7] hydrolysis of oils,[8] polymerization/depolymerization,[9] and wastewater treatment.[10,11] Most of this research is in the field of

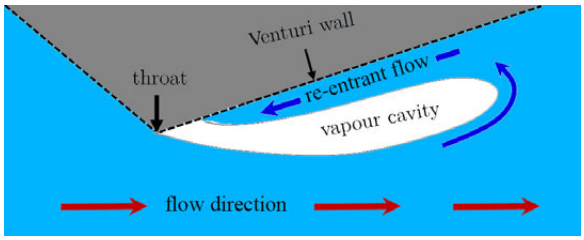

FIG. 1. Schematic of reentrant cavitation regime.

water treatment and the development of sustainable industrial activities.

The chemical effect resulting from the hydrodynamic cavitation (HC) process is the release of hydroxyl radicals (•OH) generated after the dissociation of the water molecules. These radicals strongly oxidize and can degrade organic pollutant compounds from contaminated water. The scientific literature reports a lot of research activities concerning the degradation of various organic substances,[12–14] pesticides,[15–17] pharmaceuticals,[18–25] sludge treatment,[26] bacteria, and virus disinfection.[27,28] Among the most studied applications, there is the degradation of dyes mainly from synthetic solutions, such as the Reactive Red 120 dye,[29] Brilliant Blue,[30] Congo red,[31] reactive orange 4 dye,[32] and methylene blue.[33,34]

In previous papers, the authors demonstrated hydrodynamic cavitation's efficiency in degrading methyl orange dye (MO).[35–38] MO or sodium 4-[(4-dimethylamino) phenyldiazenyl] benzenesulfonate is an azo dye soluble in water; it is used in textile production and is a residue in industrial wastewater. It is not easy to degrade MO with conventional treatment;[39] to improve the degradation efficiency, advanced oxidation processes (AOPs) are applied alone or in combination with other degradation methods. Electrochemical processes, photocatalytic oxidations, Fenton, and ultrasonic technologies are used for a partial degradation of MO.[40–42] Hybrid techniques of AOPs can be applied to increase the degradation efficiency.[42–44] However, these methods have a series of limits as the preparation of catalysts, which often requires complex operations that do not make them applicable on an industrial scale.[45] An alternative to these processes is hydrodynamic cavitation, often in combination with other processes in which chemicals substances such as hydrogen peroxide and ozone increase the number of free radicals produced that react and destroy organic pollutant molecules.[46,47]

The limitation of hydrodynamic cavitation for industrial-scale application is that there are no unique criteria for scaling up the cavitation reactor, thus restricting the applications to laboratory or pilot scale.[47] It follows that simulation tools are required to model such a phenomenon and to optimize the operating parameters.

The single bubble dynamic (SBD) models must be mentioned among the simplest approaches. They present the solution of the Rayleigh–Plesset equation for a single bubble by coupling it with continuity, momentum, and energy equations for a 1D environment.[20,48]

Numerous efforts and CFD (computational fluid dynamics) studies investigate the phenomenon of hydrodynamic cavitation. The attention is focused on many different aspects: the solution algorithm, the modeling of the gas/liquid interface, the phase transition model, the influence of turbulence, the thermal effects, the presence of incondensable gases, etc. Concerning fully Eulerian continuum approach,[49] various authors proposed research featuring the single-fluid method.[50–52] In contrast, others choose the two-fluid approach, where conservation equations are solved separately for each phase, and interaction between them is considered by using additional source terms.[53,54] Several incompressible approaches were applied for simulating cavitating flows[55–57] while compressible cavitation solvers use the so-called barotropic equation of state to relate the density of vapor–liquid mixture to the pressure field. The results obtained with such models exhibit excellent agreement with the experiments.[56,58–60]

Phase transition and gas/liquid interface modeling is relevant in cavitation CFD codes. Sauer *et al.* develop a model that exploits a simplified version of the Rayleigh–Plesset equation where the bubble growth rate is a function of saturation and local pressure.[61,62] Homogeneous equilibrium models (HEMs) compute the vapor amount present by exploiting the barotropic equation of state (EoS) and assuming a perfect mixing between the liquid and the vapor phases.[56,60,63] Homogeneous relaxation models (HRMs) are used when thermal non-equilibrium between the phases is present.[64,65]

Some other CFD codes adopt a combined Eulerian–Lagrangian approach wherein the bubbles are treated as discrete parcels. Such a modeling approach is essential when the investigation aims to resolve the physics down to the single bubble scale, maintaining computation cost affordable to capture the overall large-scale flow behavior.[66,67]

Turbulence-induced pressure fluctuations strongly influence cavitating flows.[68] Many researchers studied the mutual interaction of turbulence and cavitation with different approaches.[59,69,70] RANS (Reynolds-averaged Navier–Stokes) models, in certain conditions, overestimate turbulent viscosity in cavitation zones preventing a correct representation of reentrant jet motion.[71,72] At the same time, they predict cavitation with reasonable accuracy in high-pressure difference conditions.[73] Many other scientific works demonstrate how LES (large eddy simulation) models can adequately describe cavitation inception and evolution.[5,74,75] Detached eddy simulation (DES) approaches were also successfully used in studying cavitating flows.[55,76,77]

In specific cavitating flows, such as those issued in fuel injectors, incondensable gases and thermal effects are relevant, so various researchers focused their attention on this topic.[49,64,69,78]

In the present paper, we implemented a CFD code with an Eulerian–Lagrangian approach that solves the governing equations for a multi-phase flow in 3D domains. In the code, a finite volume approach solves the continuous field of a multi-phase mixture. We fill the continuous phase with Lagrangian particles representing the cavitation bubbles to capture the details of local pressure evolution. A specific injection model, accounting for the conditions for cavitation bubbles nucleation, ensures a proper parcel initialization. We adopted the classical fourth-order Runge–Kutta scheme to integrate the Rayleigh–Plesset equation to accurately capture the cavitation bubbles' evolution.

We first validated the CFD approach against experiments of a cavitating Venturi reactor acquired by optical imaging techniques available in the literature. In particular, we compared the numerical data with the vapor volume fraction maps obtained with computed tomography (CT). The comparison considered grid uncertainty obtained by grid refinement in the preliminary verification procedure.

Next, the decoloration of organic substances from a cavitation Venturi tube, operating at different pressure, was investigated experimentally at the Laboratory of Chemical Plants of the University of L'Aquila (Italy). Comparing the measurements with the CFD results

further verifies the proposed approach's predictive capabilities and benefits in defining the parameters that mainly affect chemical decolouration, which helps solve the scale-up problem.

II. NUMERICAL METHODOLOGY

An Eulerian–Lagrangian solver was developed in the OpenFOAM library to properly model the hydrodynamic cavitation process. The algorithm solves the continuity equation and momentum equations for the mixture,

$$\frac{\partial \rho_m}{\partial t} + \nabla \cdot (\rho_m \mathbf{U}) = 0, \tag{1}$$

$$\frac{\partial \rho_m \mathbf{U}}{\partial t} + \nabla \cdot (\rho_m \mathbf{U}\mathbf{U}) = -\nabla P + \nabla \cdot \left[(\mu_{\text{eff}} (\nabla \mathbf{U} + (\nabla \mathbf{U})^T \right], \tag{2}$$

where ρ_m is the mixture density; P is the pressure; $\mathbf{U}$ the mixture velocity; μ_{eff} is the effective viscosity.

A pressure correction equation is obtained from the continuity and momentum equations, also exploiting the equation of state for the mixture.[79,80] An iterative PIMPLE algorithm is employed within which the density and the vapor volume fraction are computed accordingly in the following equations:

$$\rho_m = (1-\gamma)\rho_l^0 + \Psi_m P, \tag{3}$$

$$\gamma = \frac{\rho_m - \rho_{l,sat}}{\rho_{v,sat} - \rho_{l,sat}}, \tag{4}$$

where γ is the vapor volume fraction ($\gamma = 0$ means no vapor; when $\gamma = 1$, a cell is filled with vapor). ρ_l^0 is a liquid reference density equal to

$$\rho_l^0 = \rho_{l,sat} - \Psi_l P_{sat}, \tag{5}$$

$\rho_{l,sat}$ and $\rho_{v,sat}$ are liquid and vapor at saturation pressure densities, respectively. Ψ_m is the mixture compressibility can be modeled in several ways. In the present work, a linear model based on vapor volume fraction was adopted,

$$\Psi_m = \gamma \Psi_v + (1-\gamma)\Psi_l. \tag{6}$$

The mixture compressibility is related to the speed of sound (a),

$$\Psi_m = \frac{1}{a^2}. \tag{7}$$

Finally, the effective viscosity is given by

$$\mu_{eff} = \mu_m + \mu_t, \tag{8}$$

where μ_t represents the turbulent viscosity modeled by a proper turbulence model. μ_m is the mixture viscosity given by

$$\mu_m = \gamma \mu_v + (1-\gamma)\mu_l. \tag{9}$$

Figure 2 compares the density values computed with the barotropic EoS for water against the real values obtained from the CoolProp database.

The Eulerian solution is coupled through the pressure field to a Lagrangian particle tracker (LPT) framework, which describes the cavitation bubbles' evolution within the domain. Each parcel represents a multitude of bubbles that share similar characteristics. Position and velocity are updated at each time step solving differential equations for trajectory and momentum,

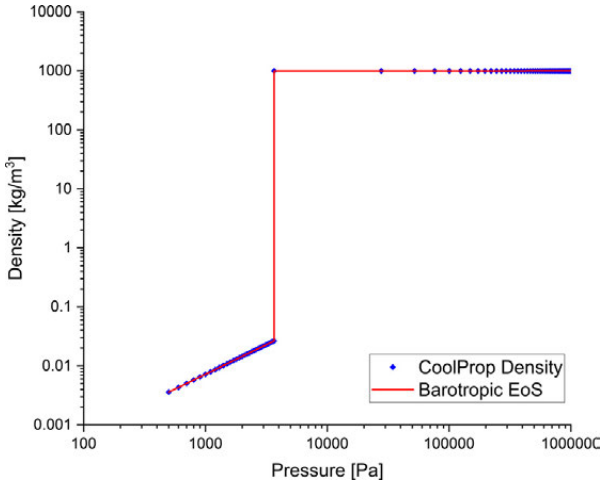

FIG. 2. Comparison of the density values computed with the adopted barotropic EoS for water against the real values obtained from the CoolProp database.

$$\frac{dx_p}{dt} = \boldsymbol{u_p}, \tag{10}$$

$$m_p \frac{du_p}{dt} = \sum \boldsymbol{F_i}, \tag{11}$$

with $\boldsymbol{u_p}$ is the parcel velocity, m_p is the mass, x_p is the position, F_i is the generic force acting on the parcels (i.e., drag, gravity, etc.).

In addition to the fundamental dynamic equations, the LPT accounts for the solution of the complete Rayleigh–Plesset equation to describe the expansion and the collapse of the vapor cavities,

$$R(t)\ddot{R}(t) + \frac{3}{2}\dot{R}^2(t) = \frac{P_B - P}{\rho_l} - 4\nu_l \frac{\dot{R}(t)}{R(t)} - \frac{2\sigma_{st}}{\rho_l R(t)}, \tag{12}$$

where $R(t), \dot{R}(t), \ddot{R}(t)$ are instantaneous radius, first and second derivatives, respectively, P is the mixture pressure, obtained from the Eulerian framework, P_B is the bubble pressure, μ_l is the liquid kinematic viscosity, σ_l is the liquid surface tension, and ρ_l is the liquid density.

The coupling with the Eulerian framework is obtained in a one-way fashion through the pressure field P, which is interpolated from the cell value for the single particle. In addition to the Rayleigh–Plesset equation, it is assumed that the bubble contains some quantity of non-condensable gas whose partial pressure is P_{Go} for some reference size R_o. Virtually all liquids have some dissolved gas. Indeed, it is impossible to eliminate this gas from any substantial liquid volume. These dissolved gases act as nucleation sites for cavitation onset. With no appreciable mass transfer between gas and liquid and thermal equilibrium, it can be demonstrated that the bubble pressure is related to the bubble radius by[48]

$$p_B(t) = P_V + P_{Go}\left(\frac{R_o}{R}\right)^{3k}, \tag{13}$$

where P_{Go} is incondensable gas partial pressure at reference conditions, R_0 is the initial bubble radius, P_V is the saturation pressure, and k is the specific heat ratio.

The Runge–Kutta fourth-order scheme integrates the Rayleigh–Plesset equation with adaptive time step. The Lagrangian time step is smaller than the Eulerian time step and dynamically changes according to the tolerance value chosen. The pressure field P used on each Runge–Kutta step is linearly interpolated from the continuous phase, using its value at the current and the previous time step. A specific injection model was developed within the solver. The model has three main input parameters:

- f_b: temporal injection frequency (s).
- n_b: bubble density, number of particle injected per volume unit ($\frac{1}{m^3}$).
- R_0: initial radius of the injected bubbles (m).

The Lagrangian particles, representative of the vapor bubbles, are injected only in those cells where there are conditions for cavitation (i.e., local pressure lower than the liquid saturation pressure). The insemination takes place with the temporal frequency f_b; for each injection event, the number of particles added is such to respect the input bubble density parameter n_b. The injection positions are randomly chosen within the eligible cells following the method implemented in OpenFOAM. For further details, see Ref. 81.

Turbulence is modeled using Spalart–Allmaras DES (detached eddy simulation).[82] This hybrid model switches between a pure LES approach in the core turbulent region where large unsteady turbulence scales can be resolved by grid size, and a RANS Spalart–Allmaras model near solid walls, where the typical length scale of the turbulent eddies is significantly smaller than the grid dimensions.

III. PRELIMINARY VALIDATION

The proposed numerical approach was validated in comparison with the experimental recordings of a hydrodynamic cavitation device acquired by Hogendoorn *et al.*[83] and Jahangir *et al.*[84,85] The shadowgraph optical technique acquired images of the flow within a Venturi tube.

CFD simulations replicate the exact geometry used in the experiments. Figure 3 reports all the characteristics of the considered Venturi tube.

OpenFOAM's utility cartesianMesh was used to discretize the geometry. Three grids were adopted: a fine grid of 0.5 mm base dimension with the throat region refined up to a dimension of 0.25 mm, an intermediate grid with dimensions of 1 mm for the base grid and 0.5 mm for the throat, and a coarse grid of 2 mm in the base grid and 1 mm in the contraction. Figure 4 shows the fine grid where the total cell count for the fine grid is 3 M.

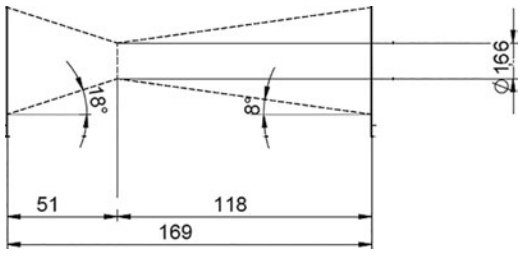

FIG. 3. Geometrical characteristics of the Venturi tube used for the code validation.

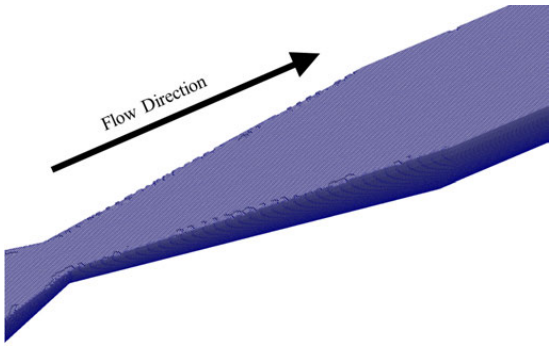

FIG. 4. Computational domain: particular view of the convergent-divergent section.

A variable time step was chosen to keep the Courant number equal to 0.25. The data for investigated conditions are reported in Table I (inlet flow rate and outflow pressure). They are representative of the two cavitation regimes previously exposed and experimentally investigated.

This combination of boundary conditions guarantees computational stability.[86,87]

Non-dimensional quantities were used to compare the experimental and CFD results. In particular, the Strouhal number St_d is used to measure the shedding frequency and is defined as follows:

$$St_d = \frac{fD}{\mathbf{U}}, \tag{14}$$

where f is the shedding frequency, D is a characteristic length considered equal to the throat diameter, and **U** is the average velocity at the throat section.

The cavitation number can express the presence of vapor and the possibility of cavitation,

$$C_v = \frac{P_2 - P_v}{\frac{1}{2}\rho \mathbf{U}^2}, \tag{15}$$

where P_2 is the downstream pressure, measured at a distance of 400 mm and sufficiently far downstream the critical section, P_v is the vapor pressure, and ρ is the reference liquid density.

In Table II, the values of these parameters obtained from the CFD simulations are compared with the one experimentally measured.

The experimental and numerical value of the Strouhal number in Table II shows that the shedding frequency is reasonably predicted for both flow conditions. Figure 5 reports the running average of pressure and velocity sampled along the axis, together with the computed uncertainty.

TABLE I. Simulated conditions parameters.

Regime	Inlet flow-rate (dm^3/s)	Outflow pressure (bar)
Reentrant jet	2.94	0.8
Condensation shock	2.99	0.4

TABLE II. Cavitation parameters and GCI.

Regime		Strouhal number	GCI	Cavitation number	GCI
Reentrant jet	Experiments	0.24	···	0.86	···
	CFD simulation	0.21	3.5%	0.88	3.2%
Condensation	Experiments	0.056	···	0.25	···
Shock	CFD simulation	0.051	3.3%	0.28	3.6%

The vertical gray line represents the throat section. The uncertainty of the numerical results was assessed as in the classical paper by Roache,[88,89] in which the uncertainty assessment procedures, now adopted by AIAA, ITTC, and IEEE are described and discussed in detail. The grid convergence index (GCI) for the Strouhal number in the two test cases is reported in Table II. The figure shows that the minimum pressure is reached downstream of the throat section and, as expected, is lower in the condensation shock mechanism. The axial velocity reaches its maximum value in the same axial position in both cases.

To verify the adequacy of the adopted grid far from the Venturi tube surface, where the turbulence model reduces to a large eddy simulation, the modeled kinetic energy was evaluated and compared with the total energy. To do that, we followed Di Mascio *et al.*[90] Figure 6 shows the ratio between the modeled kinetic energy and the total kinetic energy for the reentrant flow (top) and condensation shock regime (bottom) on the longitudinal mid-plane for a representative temporal instant.

For both conditions, the modeled kinetic energy is reasonably small in the bulk flow compared to the resolved one; the ratio between the modeled and total kinetic energy is almost everywhere smaller than the value of 0.3, and therefore, the grid can be considered adequate for LES resolution, according to the Pope criterion[91] (there are only a few spots where the latter exceeds 0.3, reaching at most 0.5). Of course, the ratio becomes larger than 0.3 in the boundary layer on the tube surfaces, where we have a Reynolds-averaged Navier–Stokes equation simulation.

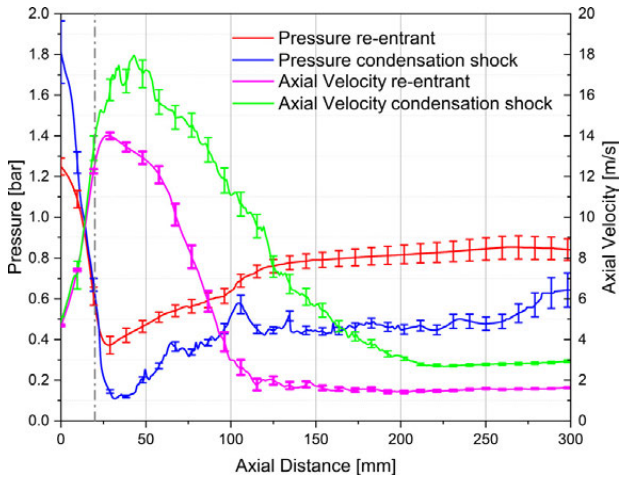

FIG. 5. Temporal averages of pressure and velocity.

Figure 7 reports a comparison of frames extracted from the high-speed images acquired with the shadowgraph technique[84,85] and the CFD simulation results for the reentrant jet shedding regime (fine grid). The high-speed shadowgraphy experiment is shown on the left while the numerical simulation is on the right. The vapor volume fraction is computed accordingly with Eq. (4).

A complete shedding cycle is reported. The numerical results for the vapor structures reasonably match the experimental observations. In particular, the numerical simulation captures the reentrant jet shedding mechanism, as seen in the velocity field reported in Fig. 8 for a shedding cycle.

The white iso-lines represent a vapor volume fraction equal to 0.1. The attached cavity grows at the contraction while the previously shed vapor flows downstream. After 2–3 ms, a cavitating vortex ring appears, with a clear reentrant jet (white zone) close to the solid boundary. As it arrives at the throat section, it splits the attached cavity from the wall shedding another vortex ring.

Figure 9 compares the numerical results with the experimental observation for the condensation shock regime (fine grid). A comparison of images demonstrates good agreement in terms of vapor

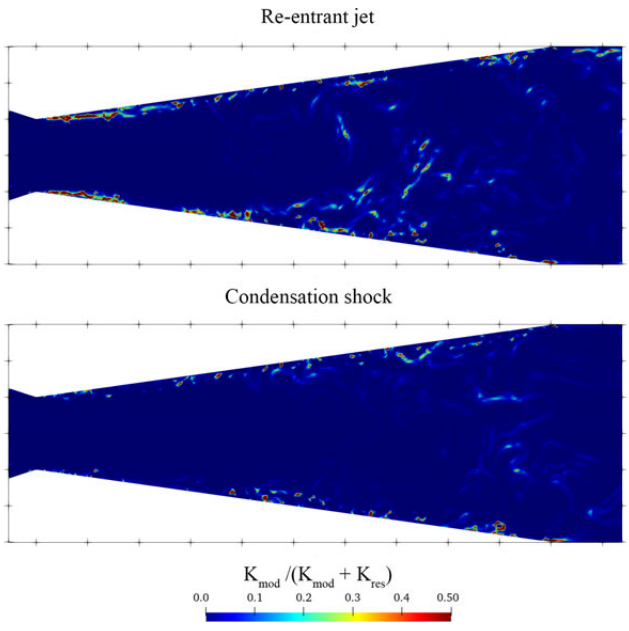

FIG. 6. $K_{mod}/(K_{mod}+K_{res})$ for reentrant jet and condensation shock regimes; longitudinal section.

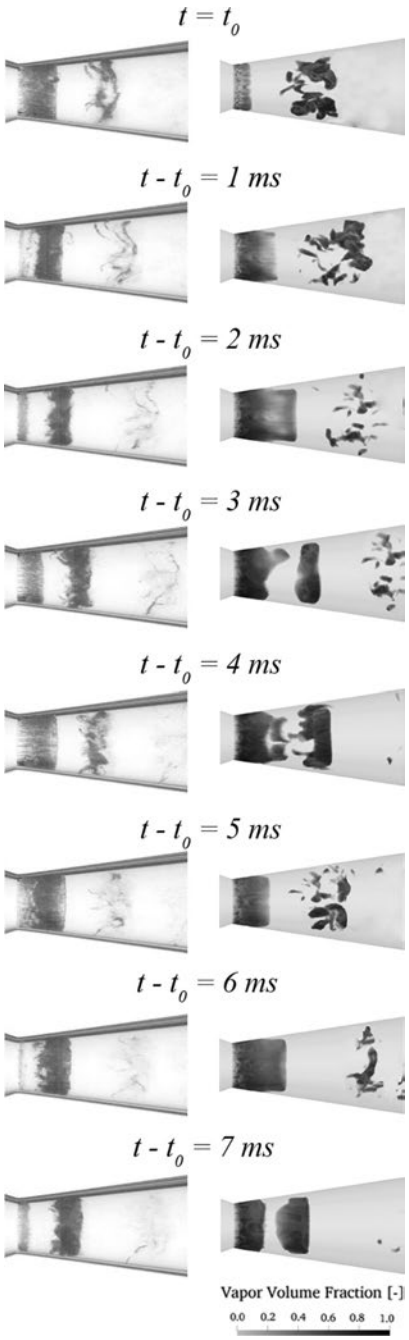

FIG. 7. Comparison of vapor volume fraction for reentrant jet conditions. Left: experimental data; right: CFD vapor volume fraction. Reproduced from Brunhart *et al.*, Phys. Fluids **32**, 083306 (2020) with the permission of AIP Publishing.[85]

distribution. As shown, the lower downstream pressure brings more extended cavitation clouds.

Computed tomography by Jahangir *et al.*[92] was used to reconstruct 2D experimental time-averaged x-ray images of the cavitating Venturi nozzle to generate a 3D quantitative representation of the averaged vapor content. The x-ray images show the average vapor distribution at different planes across the divergent section starting from the throat section and equally spaced as described in Fig. 10 (further examples of CT reconstruction can be found in Ref. 93). The CFD results for the vapor volume fraction were averaged over several shedding cycles (for the whole simulated period of 0.2 s) to compare them with the averaged CT slices.

Figure 11 compares experimental CT results to CFD images.

The agreement is satisfactory; differences can be observed only in the last slice (the farthest from the throat section), where the CFD code predicts a greater vapor cloud. It is also interesting to investigate the flow field in the condensation shock regime.

Figure 12 reports the axial velocity field with the 10% contour of volume fraction overlapped. At first, vapor shed from the previous cycle is present in the last part of the divergent duct. Vapor grows in the throat section and expands downstream until 12 ms from the beginning of the shedding cycle. Then, the condensation shock wave and the negative axial velocity detach the vapor from the walls. The negative velocity (white areas) extends even more and brings an almost complete collapse of the vapor volume attached to the walls at the end of the cycle.

IV. EXPERIMENTAL ACTIVITIES FOR DYE DECOLOURATION

Once validated, the CFD code developed was applied to study dye decolouration. This paragraph reports the experimental decoloration of methyl orange carried out at the Chemical Plants the Laboratory of the University of L'Aquila (Italy). The availability of a reliable simulation tool allows the investigation of parameters that are not available from the experiments and that are relevant for scaling up the process.

A. Chemical substances

Methyl orange dye (chemical formula: $C_{14}H_{14}N_3NaO_3S$) and sulfuric acid (98%) were provided by Carlo Erba.[94] MO was diluted in distilled water (0.1% in concentration) to prepare the synthetic solutions for experimental tests, while sulfuric acid was used to adjust the solution pH to 2 to enhance oh radical production.

B. Experimental setup and procedure

The hydrodynamic cavitation apparatus reactor is shown in Fig. 13.

The system is composed of: a jacket holding tank (maximum useful volume 1 l), a centrifugal pump of power rating 375 W and rotating speed in the range 1100–3500 rpm, manual valves, a flow meter, two electrical manometers (Barksdale Control Products, UPA2 KF16809D), and a Venturi tube. Pipelines and fittings are in plastic materials (Rilsan and polypropylene, respectively); pumps and valves are in stainless steel. The cavitation device (Venturi tube) is made of Plexiglas. Table III reports the geometrical characteristics. The tank is connected to the suction tube of the pump, and the dye solution is fluxed into the main and bypass line. A thermostatic bath connected to the tank keeps the temperature constant at 20 °C. The manometers are installed upstream and downstream of the Venturi tube and placed in the main line to measure the inlet and outlet pressure. The manual

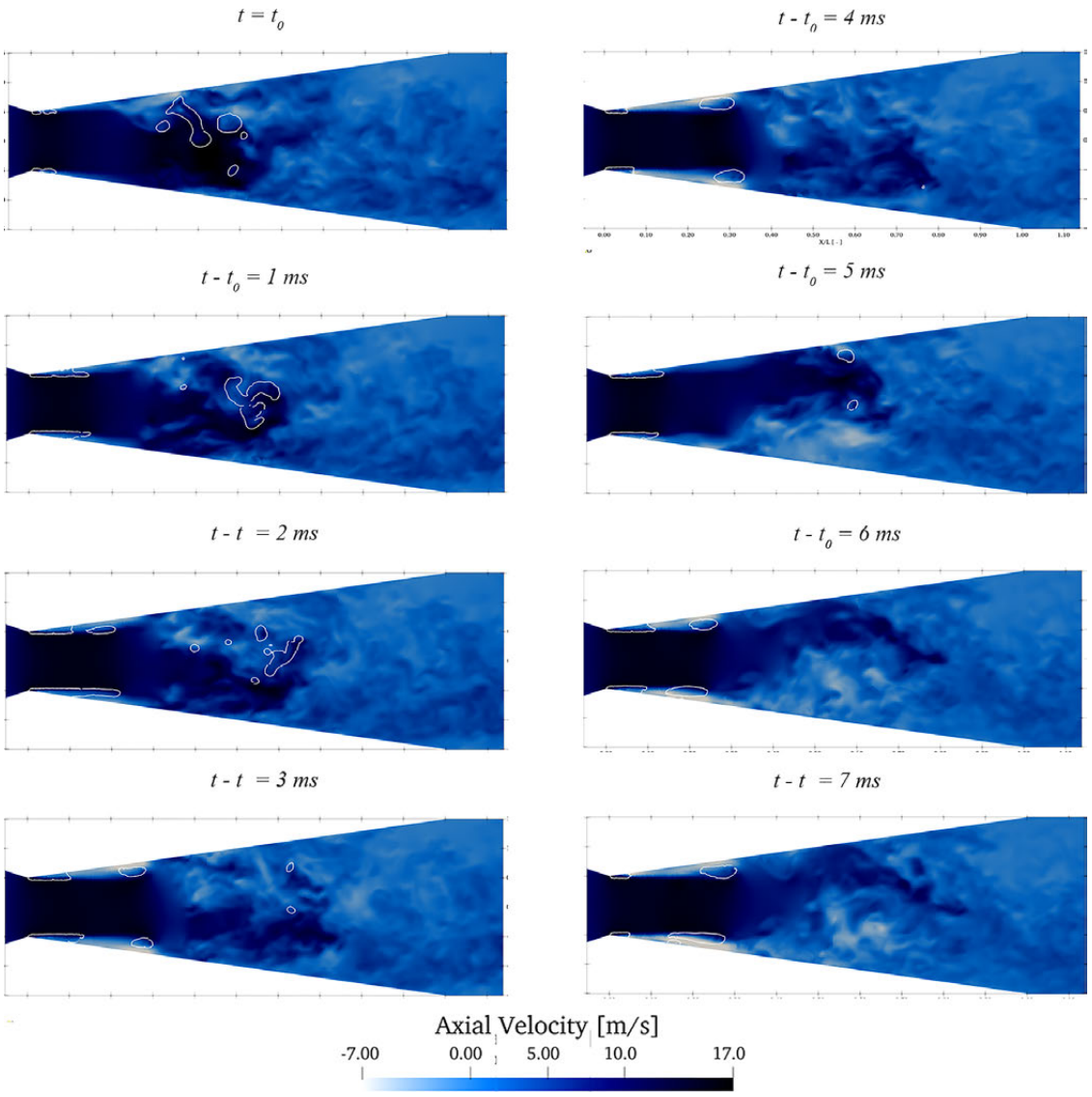

FIG. 8. Cross section of the velocity field. The volume fraction's contour line $\gamma = 0.1$ is overlapped to identify the vapor.

valves control the flow, take samples for analysis, and empty the entire plant at the end of the test.

Decoloration of MO was carried out at different inlet pressure conditions (from 3 bar min to 6 bar). A 60 min treatment time was considered, and samples for analysis were collected every 10 min. The scope of the experiments was to study the effect of the inlet pressure on the HC process and, hence, on MO decoloration. The samples were analyzed on UV-spectrometer (Cary 1E, UV Visible spectrophotometer Varian). Dye decoloration is determined as a function of absorbance reduction at the maximum wavelength of 507 nm. A calibration curve was used to measure the concentration of dye. The decoloration efficiency η was calculated by the following equation:

$$\eta = \frac{C_o - C_t}{C_o} \cdot 100, \tag{16}$$

where Co (mg/l) and Ct (mg/l) are the initial concentration and the concentration at the specific time (t), respectively. Experimental procedures for the MO degradation are also described in Refs. 35–37 and 47.

C. Experimental results

Figure 14 shows the behavior of dye decoloration efficiency and the cavitation number vs different Venturi inlet pressures (p_{in}).

The MO decoloration efficiency is approximately equal to 20% at 3, 5, and 6 bar while, at 4 bar is greater reaching its maximum value of

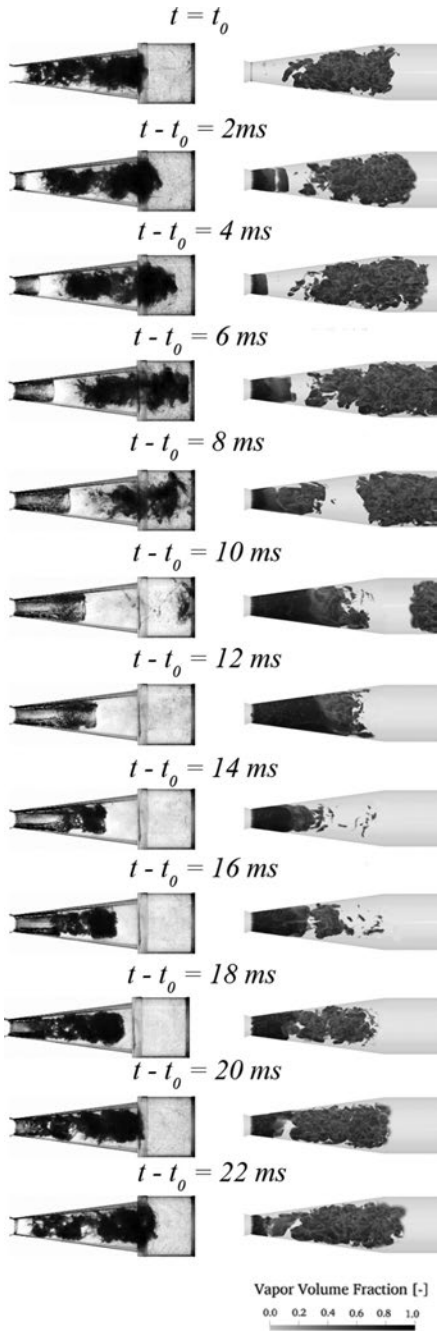

FIG. 9. Comparison of numerical data and experimental observations for condensation shock regime. Left: experimental data; right: CFD vapor volume fraction. Reproduced from Brunhart *et al.*, Phys. Fluids **32**, 083306 (2020) with the permission of AIP Publishing.[85]

32.5%. The experimental uncertainty was 1.8%, obtained by replicating the tests three times.

The cavitation number [C_ν, Eq. (15)] slightly decreases with an increasing inlet pressure.

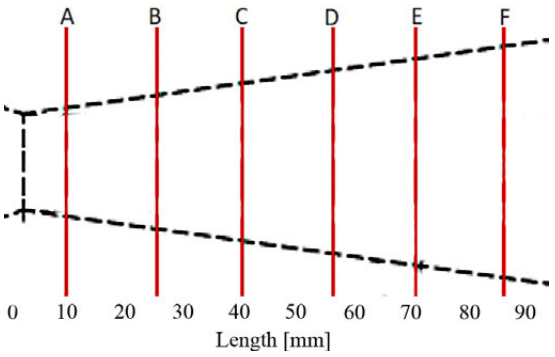

FIG. 10. Locations where computed tomography (CT) slices were taken. Letters from A to F cover 93 mm across the divergent section.

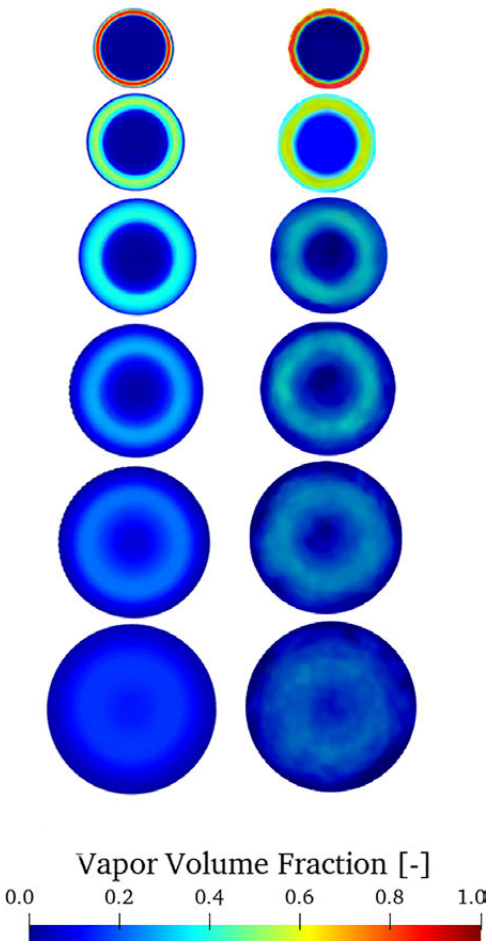

FIG. 11. Comparison of experimental observation and numerical data for the condensation shock regime. Vapor volume fraction averaged over several shedding cycles. The experimental results are obtained with computed tomography (CT). Left: experiment; right: simulation. Reproduced with permission from Jahangir *et al.*, Int. J. Multiphase Flow **120**, 103085 (2019). Copyright 2019 Elsevier.[92]

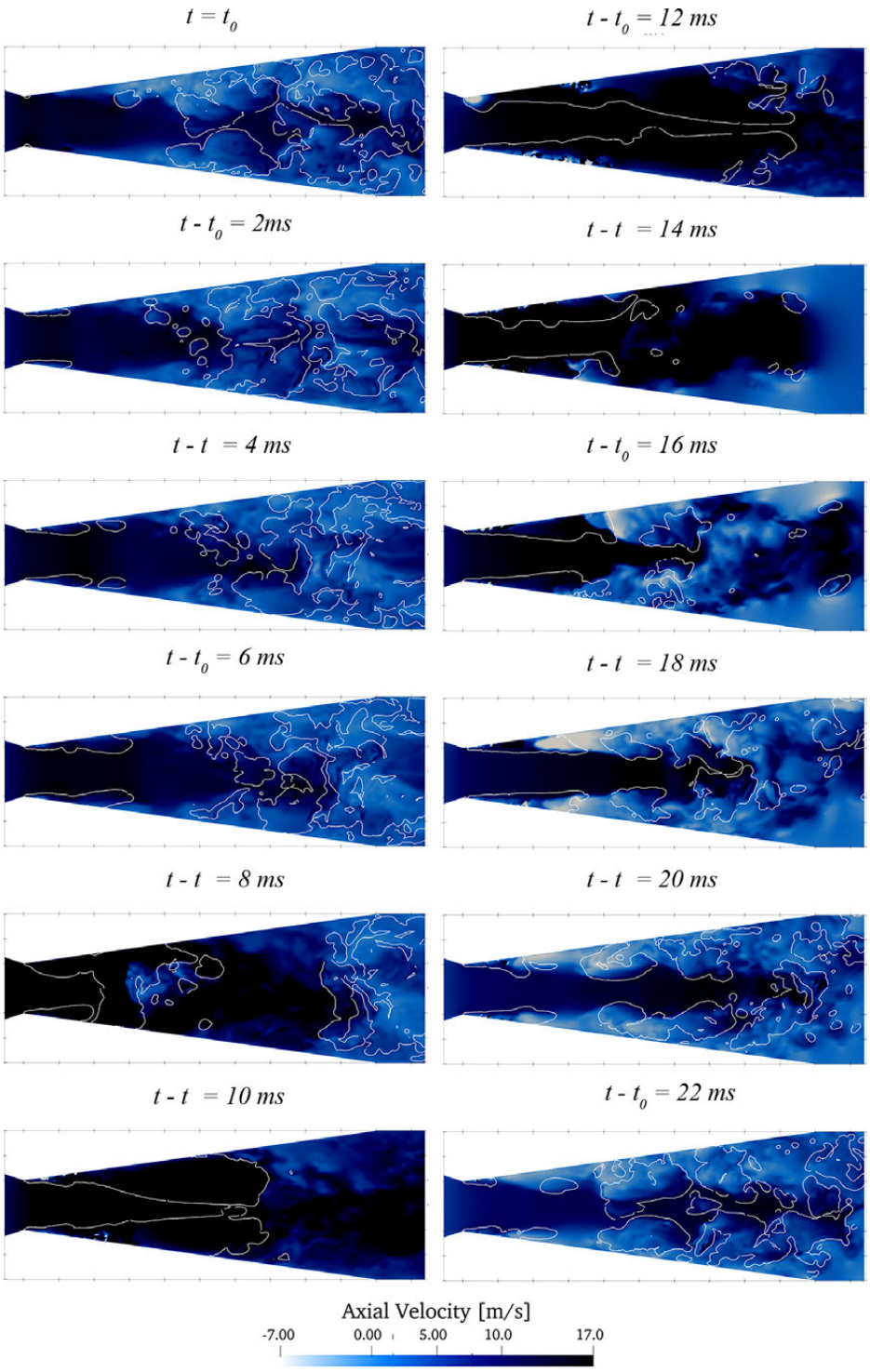

FIG. 12. Cross section of the velocity field with represented volume fraction contour $\gamma = 0.1$.

V. DYE DECOLOURATION CFD INVESTIGATION

A. Setup of simulations

The computational domain consists of a convergent-divergent geometry that reproduces the experimental device. Experimentally measured static pressure values were imposed as boundary conditions at the upstream and downstream sections of the Venturi tube, respectively. Six cases with inlet pressure ranging from 3 to 6 bar were investigated. The outlet pressure was always 1 bar. The vapor volume

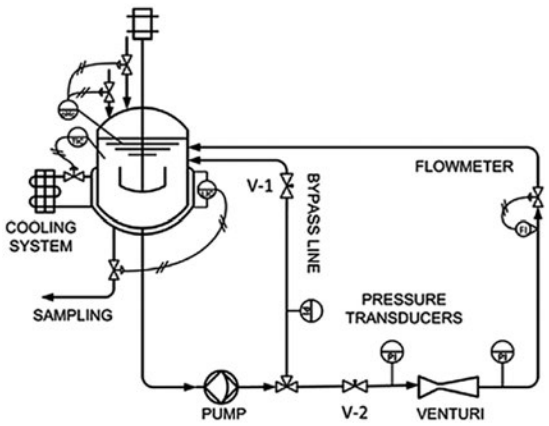

FIG. 13. Experimental apparatus adopted for the HC experiments.

TABLE III. Geometrical specifications of the Venturi tube used for hydrodynamic cavitation tests.

Venturi tube for dye decoloration (mm)	
Length of the converging	12
Length of the diverging	30
Maximum diameter	32
Orifice diameter	2

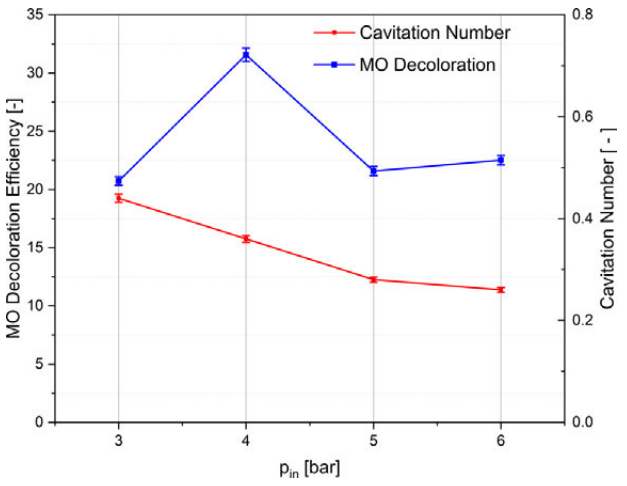

FIG. 14. MO decoloration (%) and Cavitation number as a function of inlet pressure to the Venturi tube.

fraction was set to zero at the inlet section. Figure 15 shows the grid computed with the OpenFOAM's utility cartesianMesh. Three grids were adopted: a fine grid of 0.5 mm with the throat section zone refined up to a dimension of 0.25 mm; an intermediate grid with dimensions of 1 mm, 0.5 mm for the throat section, and a coarse grid of 2–1 mm.

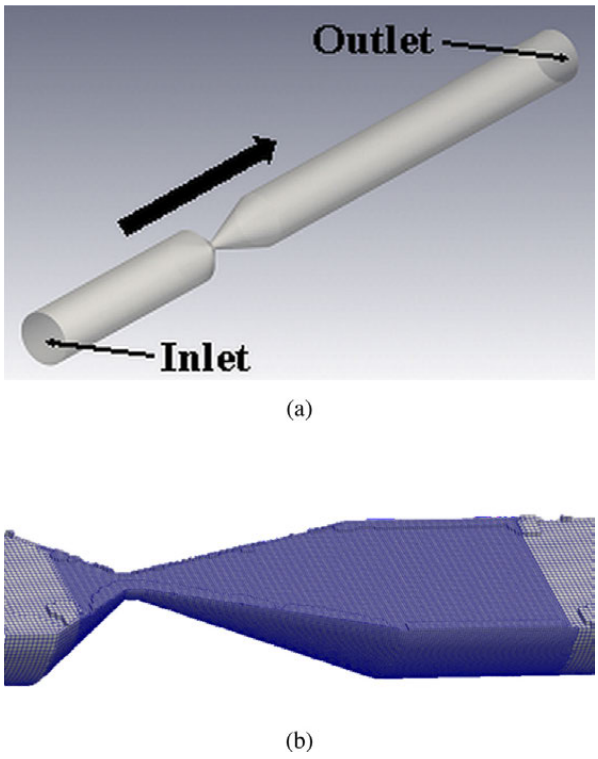

FIG. 15. Computational domain: (a) general overview and (b) particular view of the convergent-divergent section.

A variable time step was chosen to keep the Courant number below 0.25. The simulations last 0.12 s and reproduce several vapor-shedding cycles.

B. Numerical results

The different operating conditions simulated can be briefly synthesized with Strouhal and cavitation numbers as reported in Fig. 16.

Increasing the inflow pressure, both the Strouhal and cavitation number decrease. The cavitation number experimentally measured and the one computed from the CFD results are in reasonably good agreement; some differences are present only with $p_{in} = 6$ bar.

Figure 17 shows two frames experimentally acquired by Capocelli *et al.*,[20] with an ultra-fast camera using the same device investigated in this work. In the same Fig. 17, CFD simulations, at the same p_{in} conditions and at three different time steps, are reported.

The proposed numerical approach seems to properly reproduce the cavitation phenomenon experimentally observed. The cavitation process is initiated in the throat section, where bubbles nucleate on the channel's lateral surfaces. It develops in the subsequent divergent section where bubbles grow because of local low-pressure values.[22] This behavior was experimentally observed in various studies and also

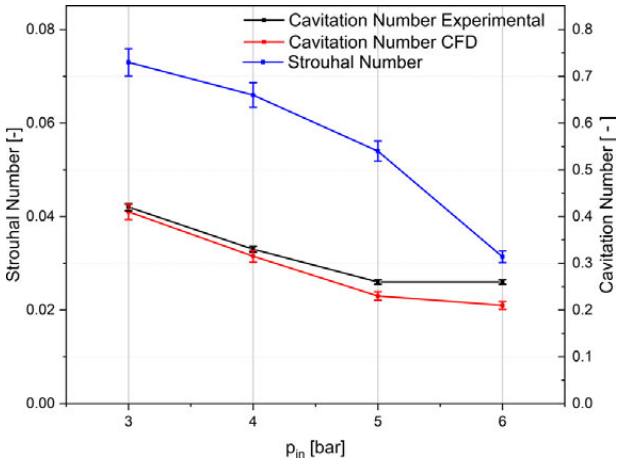

FIG. 16. Strhoual and cavitation numbers plotted against inlet pressure.

theoretically predicted.[22,48,95] It can also be observed that the higher the p_{in} is, the greater the vapor volume becomes. This is another aspect clearly visible in experimental observations of hydrodynamic cavitation by optical techniques.[48,95]

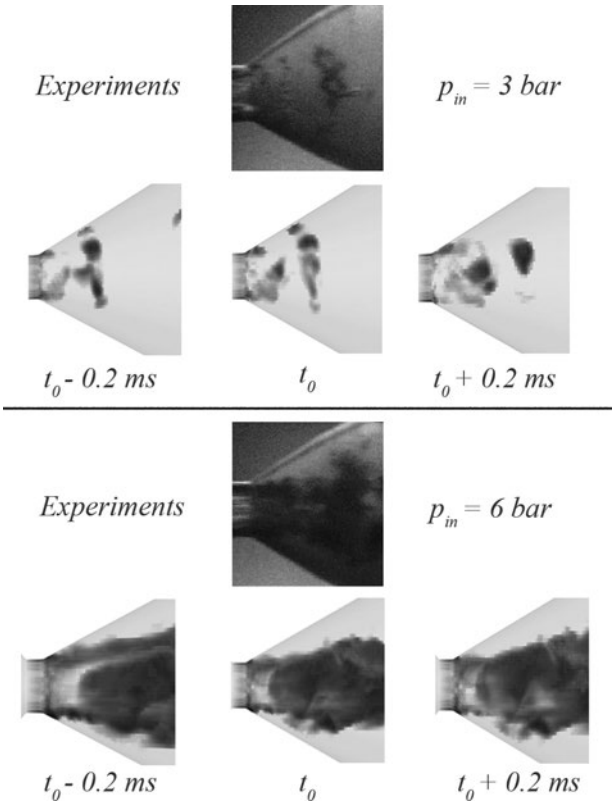

FIG. 17. Vapor volume fraction. Experimental visualization and CFD simulations for inlet pressures of 3 and 6 bar. 3 bar (a—top) and 6 bar (bottom). Reproduced with permission from Capocelli *et al.*, Chem. Eng. J. **254**, 1–8 (2014). Copyright 2014 Elsevier.[20]

Figure 18 reports the velocity field for the case with $p_{in} = 3$ and 6 bar to understand the shedding regime that is taking place in the device.

As can be clearly observed, the vapor cavities are quite short, and the white-colored areas highlight negative axial velocities; as highlighted by the volume fraction contours $\gamma = 0.1$, when increasing p_{in} the shedding mechanism remains almost unchanged.

Figure 19 reports the mean values of the number of parcels generated and the collapse peak pressure as a function of the inlet pressure. The overall averages were performed considering several shedding cycles.

As can be observed, the number of parcels increases as the inlet pressure becomes greater while the peak pressure at the bubble collapse reaches values of the order of 350 bar with minimum oscillation.

Figure 20 shows the evolution of the bubbles colored and scaled accordingly with their radius for all the inlet pressures investigated, i.e., from 3 to 6 bar.

The images start from the detachment of the bubble cloud from the throat section and show that the higher the inlet pressure, the greater the bubble cloud.

To relate this behavior with the decoloration experiments previously illustrated, it must be considered that two opposite effects co-exist when increasing the inlet pressure: greater vapor clouds appear, but, at the same time, the coalescence phenomenon is enhanced too. At first, with relatively low inlet pressure, the bubbles, where hydrolysis can occur, are very few and, as a consequence, the OH radicals production is very low (Fig. 20, $p_{in} = 3$). Increasing the p_{in} the presence of more bubbles has a positive effect enhancing the decoloration efficiency, while coalescence effects are still secondary (Fig. 20, $p_{in} = 4$). Finally, if an excessively high inlet pressure is adopted, the bubble density becomes so high that these cavities coalesce to form much larger cavitation bubbles where recombination of oxidizing radicals takes place (Fig. 20, $p_{in} = 5 - 6$). This behavior was already discussed by various researchers in the field, demonstrating the presence of an optimal operating condition for the hydrodynamic cavitation as a method for chemical substances treatment.[96–99] Hence, this condition should be a trade-off between these two opposite tendencies previously discussed.

VI. CONCLUSIONS

A combined numerical–experimental analysis of the hydrodynamic cavitation process was carried out. A Eulerian–Lagrangian code purposely developed for hydrodynamic cavitation processes was successfully implemented within the OpenFOAM library. It features an LPT framework to follow the bubble's development within the integration domain and, in particular, the complete solution of the Rayleigh–Plesset equation to calculate the vapor's bubble diameter evolution.

This CFD code was validated against comprehensive experimental data acquired with the shadowgraph optical technique of a cavitating Venturi tube. Both reentrant jet and condensation shock-shedding mechanisms were considered. Computed tomography data of vapor volume fraction in the divergent section were also considered for a quantitative comparison with numerical results.

The decoloration of organic substances with hydrodynamic cavitation was also investigated. Initially, an experimental campaign was

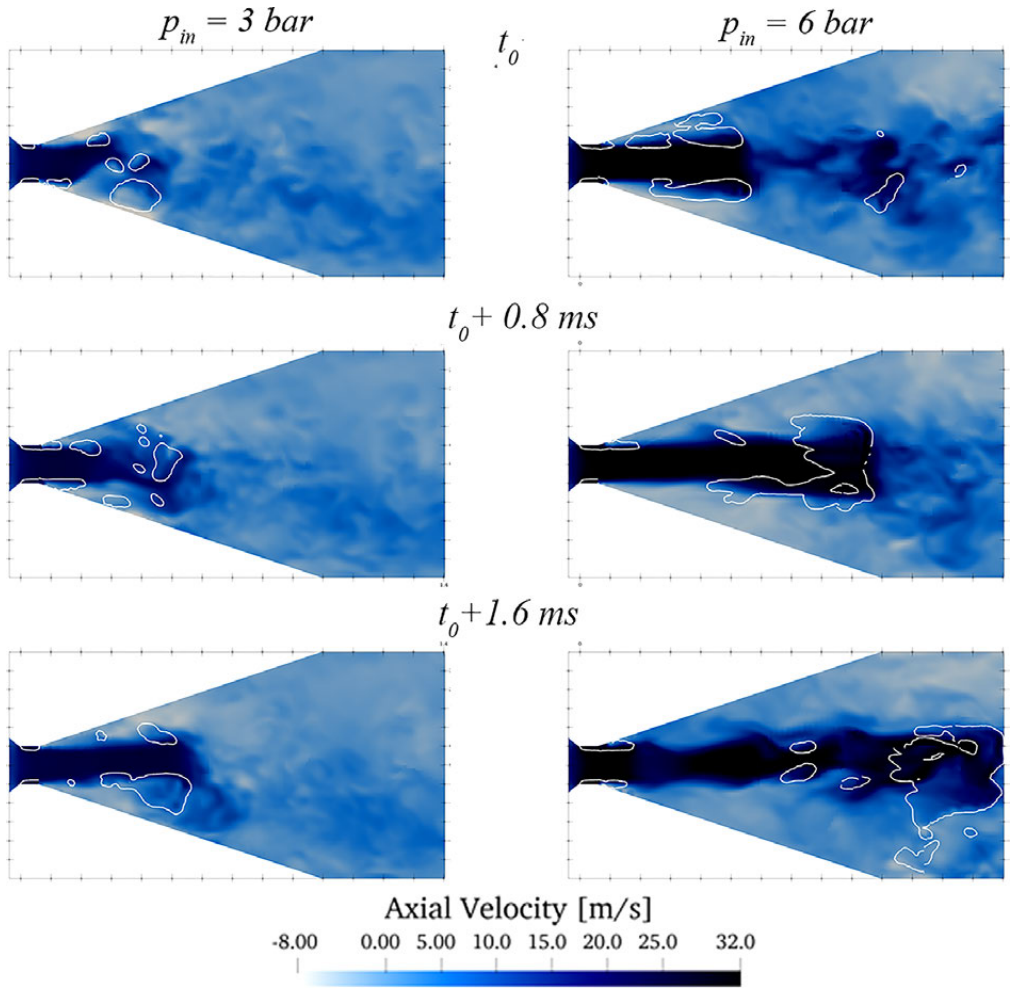

FIG. 18. Mid-plane cross-section with represented vapor volume fraction iso-lines at 10% over-imposed to an axial velocity plot for p_{in} = 3 and 6 bar.

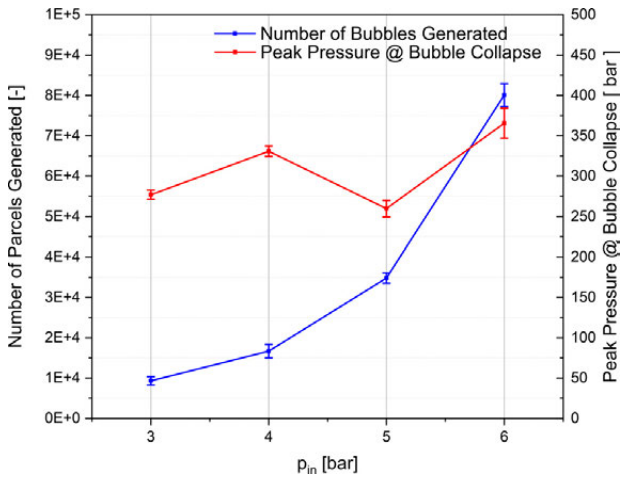

FIG. 19. Peak pressure at bubble collapse and number of parcels present in their domain for p_{in} = 3–6 bar.

performed using methyl orange in synthetic aqueous solutions. Various experiments were performed to change the inlet pressure. The results showed the effects of this parameter on dye decolouration. In particular, it was found that the highest HC process efficiency was recorded at 4 bar inlet pressure with a MO decoloration yield of 32% while, for lower (3 bar) and higher inlet pressures (5 and 6 bar), the efficiency is about 20%.

Then, the developed code was tested on the same geometry experimentally investigated. The main findings are:

- The numerical approach adopted is capable of reproducing the cavitation process experimentally analyzed as shown by both image and a-dimensional numbers comparisons.
- When increasing the upstream pressure, both Strouhal and cavitation number decrease.
- The bubble formation begins on the lateral surfaces of the throat section. The bubbles flow in the divergent section collapse and reach an average peak pressure of 300–400 bar, depending on the inlet pressure.

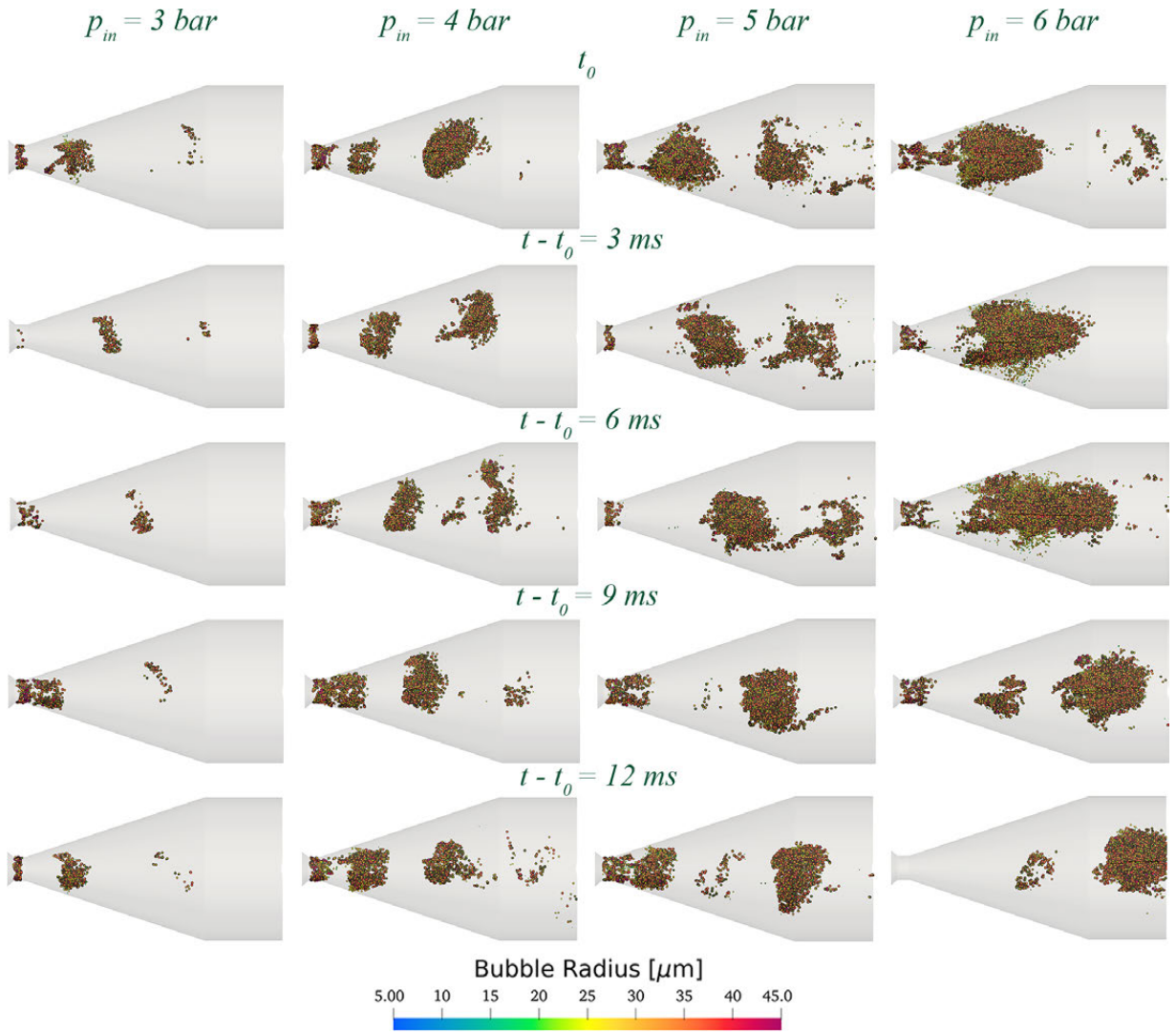

FIG. 20. Bubble evolution for p_{in} = 3–6 bar.

- The bubble cloud reproduced by the CFD code becomes more extended as the inlet pressure increase. However, the coalescence phenomenon plays an important role because it triggers the radicals' recombination diminishing the decoloration efficiency.

Finally, the CFD code exhibits a good predictive capability and can be used to assess scale-up criteria for possible industrial applications of hydrodynamic cavitation. Future works will regard the investigation of scaled-up applications, different geometries, and operating conditions as well as the implementation of a coalescence model to better represent the process of the radicals' recombination.

ACKNOWLEDGMENTS

All the simulations were performed with the developed solver on the Galileo100 cluster of HPC CINECA facilities within the agreement between DIIIE-Università degli Studi dell'Aquila and CINECA.

AUTHOR DECLARATIONS

Conflict of Interest

The authors have no conflicts to disclose.

Author Contributions

Francesco Duronio: Conceptualization (lead); Investigation (equal); Methodology (lead); Software (lead); Validation (equal); Visualization (equal); Writing – original draft (lead). **Andrea Di Mascio:** Conceptualization (equal); Methodology (equal); Supervision (equal); Writing – original draft (equal); Writing – review & editing (equal). **Angelo De Vita:** Methodology (equal); Project administration

(equal); Supervision (equal); Writing – original draft (equal); Writing – review & editing (equal). **Valentina Innocenzi:** Conceptualization (equal); Investigation (lead); Validation (equal); Writing – original draft (equal); Writing – review & editing (equal). **Marina Prisciandaro:** Investigation (equal); Project administration (equal); Resources (equal); Supervision (equal); Writing – review & editing (equal).

DATA AVAILABILITY

The data that support the findings of this study are available within the article.

REFERENCES

[1]U. Gawandalkar and C. Poelma, "The structure of near-wall re-entrant flow and its influence on cloud cavitation instability," Exp. Fluids **63**, 77 (2022).
[2]R. A. Furness and S. P. Hutton, "Experimental and theoretical studies of two-dimensional fixed-type cavities," J. Fluids Eng. **97**, 515–521 (1975).
[3]J. K. Jakobsen, "On the mechanism of head breakdown in cavitating inducers," J. Basic Eng. **86**, 291–305 (1964).
[4]C. Wang, B. Huang, G. Wang, M. Zhang, and N. Ding, "Unsteady pressure fluctuation characteristics in the process of breakup and shedding of sheet/cloud cavitation," Int. J. Heat Mass Transfer **114**, 769–785 (2017).
[5]B. Budich, S. J. Schmidt, and N. A. Adams, "Numerical simulation and analysis of condensation shocks in cavitating flow," J. Fluid Mech. **838**, 759–813 (2018).
[6]K. R. Laberteaux and S. L. Ceccio, "Partial cavity flows. Part 1. Cavities forming on models without spanwise variation," J. Fluid Mech. **431**, 1–41 (2001).
[7]V. Innocenzi and M. Prisciandaro, "Technical feasibility of biodiesel production from virgin oil and waste cooking oil: Comparison between traditional and innovative process based on hydrodynamic cavitation," Waste Manage. **122**, 15–25 (2021).
[8]A. B. Pandit and J. B. Joshi, "Hydrolysis of fatty oils: Effect of cavitation," Chem. Eng. Sci. **48**, 3440–3442 (1993).
[9]V. S. Moholkar, P. S. Kumar, and A. B. Pandit, "Hydrodynamic cavitation for sonochemical effects," Ultrason. Sonochem. **6**, 53–65 (1999).
[10]M. Gągol, A. Przyjazny, and G. Boczkaj, "Wastewater treatment by means of advanced oxidation processes based on cavitation—A review," Chem. Eng. J. **338**, 599–627 (2018).
[11]Y. Tao, J. Cai, X. Huai, B. Liu, and Z. Guo, "Application of hydrodynamic cavitation to wastewater treatment," Chem. Eng. Technol. **39**, 1363–1376 (2016).
[12]V. Innocenzi, M. Prisciandaro, and F. Vegliò, "Effect of the hydrodynamic cavitation for the treatment of industrial wastewater," Chem. Eng. Trans. **67**, 529–534 (2018).
[13]P. Thanekar and P. Gogate, "Application of hydrodynamic cavitation reactors for treatment of wastewater containing organic pollutants: Intensification using hybrid approaches," Fluids **3**, 98 (2018).
[14]S. Raut-Jadhav, M. P. Badve, D. V. Pinjari, D. R. Saini, S. H. Sonawane, and A. Pandit, "Treatment of the pesticide industry effluent using hydrodynamic cavitation and its combination with process intensifying additives (H_2O_2 and ozone)," Chem. Eng. J. **295**, 326–335 (2016).
[15]S. Raut-Jadhav, D. Saini, S. Sonawane, and A. Pandit, "Effect of process intensifying parameters on the hydrodynamic cavitation based degradation of commercial pesticide (methomyl) in the aqueous solution," Ultrason. Sonochem. **28**, 283–293 (2016).
[16]R. K. Joshi and P. R. Gogate, "Degradation of dichlorvos using hydrodynamic cavitation based treatment strategies," Ultrason. Sonochem. **19**, 532–539 (2012).
[17]B. Li, S. Li, L. Yi, H. Sun, J. Qin, J. Wang, and D. Fang, "Degradation of organophosphorus pesticide diazinon by hydrodynamic cavitation: Parameters optimization and mechanism investigation," Process Saf. Environ. Prot. **153**, 257–267 (2021).
[18]D. Panda and S. Manickam, "Hydrodynamic cavitation assisted degradation of persistent endocrine-disrupting organochlorine pesticide dicofol: Optimization of operating parameters and investigations on the mechanism of intensification," Ultrason. Sonochem. **51**, 526–532 (2019).
[19]M. Zupanc, T. Kosjek, M. Petkovšek, M. Dular, B. Kompare, B. Širok, M. Strazar, and E. Heath, "Shear-induced hydrodynamic cavitation as a tool for pharmaceutical micropollutants removal from urban wastewater," Ultrason. Sonochem. **21**, 1213–1221 (2014).
[20]M. Capocelli, M. Prisciandaro, A. Lancia, and D. Musmarra, "Hydrodynamic cavitation of p-nitrophenol: A theoretical and experimental insight," Chem. Eng. J. **254**, 1–8 (2014).
[21]D. Musmarra, M. Prisciandaro, M. Capocelli, D. Karatza, P. Iovino, S. Canzano, and A. Lancia, "Degradation of ibuprofen by hydrodynamic cavitation: Reaction pathways and effect of operational parameters," Ultrason. Sonochem. **29**, 76–83 (2016).
[22]M. Capocelli, D. Musmarra, M. Prisciandaro, and A. Lancia, "Chemical effect of hydrodynamic cavitation: Simulation and experimental comparison," AIChE J. **60**, 2566–2572 (2014).
[23]J. Lalwani, A. Gupta, S. Thatikonda, and C. Subrahmanyam, "Oxidative treatment of crude pharmaceutical industry effluent by hydrodynamic cavitation," J. Environ. Chem. Eng. **8**, 104281 (2020).
[24]M. V. Bagal and P. R. Gogate, "Degradation of diclofenac sodium using combined processes based on hydrodynamic cavitation and heterogeneous photocatalysis," Ultrason. Sonochem. **21**(3), 1035–1043 (2014).
[25]G. Mancuso, M. Langone, G. Andreottola, and L. Bruni, "Effects of hydrodynamic cavitation, low-level thermal and low-level alkaline pre-treatments on sludge solubilisation," Ultrason. Sonochem. **59**, 104750 (2019).
[26]Š. Zezulka, E. Maršálková, F. Pochylý, P. Rudolf, M. Hudec, and B. Maršálek, "High-pressure jet-induced hydrodynamic cavitation as a pre-treatment step for avoiding cyanobacterial contamination during water purification," J. Environ. Manage. **255**, 109862 (2020).
[27]K. K. Jyoti and A. B. Pandit, "Water disinfection by acoustic and hydrodynamic cavitation," Biochem. Eng. J. **7**, 201–212 (2001).
[28]V. K. Saharan, M. P. Badve, and A. B. Pandit, "Degradation of reactive red 120 dye using hydrodynamic cavitation," Chem. Eng. J. **178**, 100–107 (2011).
[29]S. Baradaran and M. T. Sadeghi, "Coomassie brilliant blue (CBB) degradation using hydrodynamic cavitation hydrogen peroxide and activated persulfate (HC-H_2O_2-KPS) combined process," Chem. Eng. Process.-Process Intensif. **145**(145), 107674 (2019).
[30]Z. Askarniya, M.-T. Sadeghi, and S. Baradaran, "Decolorization of congo red via hydrodynamic cavitation in combination with fenton's reagent," Chem. Eng. Process.-Process Intensif. **150**, 107874 (2020).
[31]M. M. Gore, V. K. Saharan, D. V. Pinjari, P. V. Chavan, and A. Pandit, "Degradation of reactive orange dye using hydrodynamic cavitation based hybrid techniques," Ultrason. Sonochem. **21**(4), 1075–1082 (2014).
[32]B. Wang, T. Wang, and H. Su, "A dye-methylene blue (MB)-degraded by hydrodynamic cavitation (HC) and combined with other oxidants," J. Environ. Chem. Eng. **10**, 107877 (2022).
[33]M. S. Kumar, S. H. Sonawane, and A. Pandit, "Degradation of methylene blue dye in aqueous solution using hydrodynamic cavitation based hybrid advanced oxidation processes," Chem. Eng. Process.: Process Intensif. **122**, 288–295 (2017).
[34]J. P. Guin, Y. K. Bhardwaj, and L. Varshney, "Mineralization and biodegradability enhancement of methyl orange dye by an effective advanced oxidation process," Appl. Radiat. Isot. **122**, 153–157 (2017).
[35]V. Innocenzi, M. Prisciandaro, and F. Vegliò, "Study of the effect of operative conditions on the decolourization of azo dye solutions by using hydrodynamic cavitation at the lab scale," Can. J. Chem. Eng. **98**, 1980–1988 (2020).
[36]V. Innocenzi, M. Prisciandaro, F. Tortora, and F. Vegliò, "Optimization of hydrodynamic cavitation process of azo dye reduction in the presence of metal ions," J. Environ. Chem. Eng. **6**, 6787–6796 (2018).
[37]V. Innocenzi, M. Prisciandaro, M. Centofanti, and F. Vegliò, "Comparison of performances of hydrodynamic cavitation in combined treatments based on hybrid induced advanced fenton process for degradation of azo-dyes," J. Environ. Chem. Eng. **7**, 103171 (2019).
[38]Z. Abbas-Shiroodi, M.-T. Sadeghi, and S. Baradaran, "Design and optimization of a cavitating device for congo red decolorization: Experimental investigation and CFD simulation," Ultrason. Sonochem. **71**, 105386 (2021).
[39]Y. L. Pang, A. Z. Abdullah, and S. Bhatia, "Review on sonochemical methods in the presence of catalysts and chemical additives for treatment of organic pollutants in wastewater," Desalination **277**, 1–14 (2011).

[40]J. Luo, X. Zhou, L. Ma, X. Xu, J. Wu, and H. Liang, "Enhanced photodegradation activity of methyl orange over Ag_2CrO_4/SnS_2 composites under visible light irradiation," Mater. Res. Bull. **77**, 291–299 (2016).
[41]I. M. S. Pillai and A. K. Gupta, "Effect of inorganic anions and oxidizing agents on electrochemical oxidation of methyl orange, malachite green and 2,4-dinitrophenol," J. Electroanal. Chem. **762**, 66–72 (2016).
[42]R. Mohammadi and M. Mohammadi, "Photocatalytic removal of methyl orange using Ag/Zn–TiO_2 nanoparticles prepared by different methods," Desalin. Water Treat. **57**, 11317–11325 (2016).
[43]M. Hassanpour, H. Safardoust, D. Ghanbari, and M. Salavati-Niasari, "Microwave synthesis of CuO/NiO magnetic nanocomposites and its application in photo-degradation of methyl orange," J. Mater. Sci.: Mater. Electron. **27**, 2718–2727 (2016).
[44]S. Yang, R. Jin, Z. He, Y. Qiao, S. Shi, W. Kong, Y. Wang, and X. Liu, "An experimental study on the degradation of methyl orange by combining hydrodynamic cavitation and chlorine dioxide treatments," Chem. Eng. Trans. **59**, 289–294 (2017).
[45]S. Das, A. P. Bhat, and P. R. Gogate, "Degradation of dyes using hydrodynamic cavitation: Process overview and cost estimation," J. Water Process Eng. **42**, 102126 (2021).
[46]B. Wang, H. Su, and B. Zhang, "Hydrodynamic cavitation as a promising route for wastewater treatment—A review," Chem. Eng. J. **412**, 128685 (2021).
[47]V. Innocenzi, A. Colangeli, and M. Prisciandaro, "Methyl orange decolourization through hydrodynamic cavitation in high salinity solutions," Chem. Eng. Process.-Process Intensif. **179**, 109050 (2022).
[48]C. E. Brennen, *Cavitation and Bubble Dynamics* (Cambridge University Press, 2013).
[49]S. Yang and C. Habchi, "Real-fluid phase transition in cavitation modeling considering dissolved non-condensable gas," Phys. Fluids **32**, 032102 (2020).
[50]F. Giussani, F. Piscaglia, G. Saez-Mischlich, and J. Hèlie, "A three-phase VOF solver for the simulation of in-nozzle cavitation effects on liquid atomization," J. Comput. Phys. **406**, 109068 (2020).
[51]Y. Chen, X. Chen, J. Li, Z. Gong, and C. Lu, "Large eddy simulation and investigation on the flow structure of the cascading cavitation shedding regime around 3D twisted hydrofoil," Ocean Eng. **129**, 1–19 (2017).
[52]M. Gavaises, F. Villa, P. Koukouvinis, M. Marengo, and J.-P. Franc, "Visualisation and LES simulation of cavitation cloud formation and collapse in an axisymmetric geometry," Int. J. Multiphase Flow **68**, 14–26 (2015).
[53]H. Liu, W. Zhang, M. Jia, Y. Yan, and Y. He, "An improved method for coupling the in-nozzle cavitation with multi-fluid-quasi-VOF model for diesel spray," Comput. Fluids **177**, 20–32 (2018).
[54]W. Yuan and G. H. Schnerr, "Numerical simulation of two-phase flow in injection nozzles: Interaction of cavitation and external jet formation," J. Fluids Eng. **125**, 963–969 (2003).
[55]R. E. Bensow and G. Bark, "Implicit LES predictions of the cavitating flow on a propeller," J. Fluids Eng. **132**, 041302 (2010).
[56]M. S. Mihatsch, S. J. Schmidt, and N. A. Adams, "Cavitation erosion prediction based on analysis of flow dynamics and impact load spectra," Phys. Fluids **27**, 103302 (2015).
[57]M. Cristofaro, W. Edelbauer, P. Koukouvinis, and M. Gavaises, "A numerical study on the effect of cavitation erosion in a diesel injector," Appl. Math. Modell. **78**, 200–216 (2020).
[58]A. Žnidarčič, R. Mettin, and M. Dular, "Modeling cavitation in a rapidly changing pressure field—Application to a small ultrasonic horn," Ultrason. Sonochem. **22**, 482–492 (2015).
[59]P. Koukouvinis, H. Naseri, and M. Gavaises, "Performance of turbulence and cavitation models in prediction of incipient and developed cavitation," Int. J. Engine Res. **18**, 333–350 (2017).
[60]N. Kyriazis, P. Koukouvinis, and M. Gavaises, "Modelling cavitation during drop impact on solid surfaces," Adv. Colloid Interface Sci. **260**, 46–64 (2018).
[61]J. Sauer and G. H. Schnerr, "Development of a new cavitation model based on bubble dynamics," J. Appl. Math. Mech. /Z. Angew. Math. Mech. **81**, 561–562 (2001).
[62]W. Yuan, J. Sauer, and G. H. Schnerr, "Modeling and computation of unsteady cavitation flows in injection nozzles," Méc. Ind. **2**, 383–394 (2001).
[63]See https://asmedigitalcollection.asme.org/FEDSM/proceedings-pdf/FEDSM2007/42894/465/2669848/465_1.pdf for Modelling Injector Flow Including Cavitation Effects for Diesel Applications, Fluids Engineering Division Summer Meeting, Vol. 2: Fora, Parts A and B (2007).
[64]M. Battistoni, D. Duke, A. B. Swantek, F. Z. Tilocco, C. F. Powell, and S. Som, "Effects of noncondensable gas on cavitating nozzles," Atomization Sprays **25**, 453–483 (2015).
[65]F. Duronio, A. Di Mascio, C. Villante, M. Anatone, and A. De Vita, "ECN spray G: Coupled eulerian internal nozzle flow and Lagrangian spray simulation in flash boiling conditions," Int. J. Engine Res. **24**(4), 1530–1544 (2023).
[66]J. Ma, C.-T. Hsiao, and G. L. Chahine, "Euler–Lagrange simulations of bubble cloud dynamics near a wall," J. Fluids Eng. **137**, 041301 (2015).
[67]E. Giannadakis, M. Gavaises, and C. Arcoumanis, "Modelling of cavitation in diesel injector nozzles," J. Fluid Mech. **616**, 153–193 (2008).
[68]W. Edelbauer, J. Strucl, and A. Morozov, "Large eddy simulation of cavitating throttle flow," in *Advances in Hydroinformatics* (Springer-Verlag, 2016).
[69]G. Strotos, P. Koukouvinis, A. Theodorakakos, M. Gavaises, and G. Bergeles, "Transient heating effects in high pressure diesel injector nozzles," Int. J. Heat Fluid Flow **51**, 257–267 (2015).
[70]C. O. Iyer and S. L. Ceccio, "The influence of developed cavitation on the flow of a turbulent shear layer," Phys. Fluids **14**, 3414–3431 (2002).
[71]M. Dular and O. Coutier-Delgosha, "Numerical modelling of cavitation erosion," Int. J. Numer. Methods Fluids **61**, 1388–1410 (2009).
[72]O. Coutier-Delgosha, R. Fortes-Patella, and J. L. Reboud, "Evaluation of the turbulence model influence on the numerical simulations of unsteady cavitation," J. Fluids Eng. **125**, 38–45 (2003).
[73]A. Morozov, J. Struci, and W. Edelbauer, "Large eddy simulation of cavitating throttle flow," in *Proceedings of the SimHydro 2014. New Trends in Simulation, 11–13 June 2014* (Ecole Polytech', Nice, France, 2014).
[74]M. H. Arabnejad, A. Amini, M. Farhat, and R. E. Bensow, "Numerical and experimental investigation of shedding mechanisms from leading-edge cavitation," Int. J. Multiphase Flow **119**, 123–143 (2019).
[75]X. Long, H. Cheng, B. Ji, R. E. Arndt, and X. Peng, "Large eddy simulation and Euler–Lagrangian coupling investigation of the transient cavitating turbulent flow around a twisted hydrofoil," Int. J. Multiphase Flow **100**, 41–56 (2018).
[76]P. K. Ullas, D. Chatterjee, and S. Vengadesan, "Prediction of unsteady, internal turbulent cavitating flow using dynamic cavitation model," Int. J. Numer. Methods Heat Fluid Flow **32**, 3210–3232 (2022).
[77]O. Usta and E. Korkut, "A study for cavitating flow analysis using des model," Ocean Eng. **160**, 397–411 (2018).
[78]F. Orley, S. Hickel, S. J. Schmidt, and N. A. Adams, "Large-eddy simulation of turbulent, cavitating fuel flow inside a 9-hole diesel injector including needle movement," Int. J. Engine Res. **18**, 195–211 (2017).
[79]J. H. Ferziger, M. Perić, and R. L. Street, *Computational Methods for Fluid Dynamics* (Springer, 2002), Vol. 3.
[80]M. Darwish and F. Moukalled, *The Finite Volume Method in Computational Fluid Dynamics: An Advanced Introduction with OpenFOAM® and Matlab®* (Springer, 2016).
[81]C. J. Greenshields *et al.*, "Openfoam user guide version 6," OpenFOAM Found. **237**, 624 (2018).
[82]P. R. Spalart, S. Deck, M. L. Shur, K. D. Squires, M. K. Strelets, and A. Travin, "A new version of detached-eddy simulation, resistant to ambiguous grid densities," Theor. Comput. Fluid Dyn. **20**, 181 (2006).
[83]W. Hogendoorn, "Cavitation: Experimental investigation of cavitation regimes in a coverging-diverging nozzle," M.S. thesis [Delft University of Technology (TU Delft), 2017].
[84]S. Jahangir, W. Hogendoorn, and C. Poelma, "Dynamics of partial cavitation in an axisymmetric converging-diverging nozzle," Int. J. Multiphase Flow **106**, 34–45 (2018).
[85]M. Brunhart, C. Soteriou, M. Gavaises, I. Karathanassis, P. Koukouvinis, S. Jahangir, and C. Poelma, "Investigation of cavitation and vapor shedding mechanisms in a venturi nozzle," Phys. Fluids **32**, 083306 (2020).
[86]H. K. Versteeg and W. Malalasekera, *An Introduction to Computational Fluid Dynamics: The Finite Volume Method* (Pearson Education, 2007).
[87]F. Duronio, A. Montanaro, L. Allocca, S. Ranieri, and A. De Vita, "Effects of thermodynamic conditions and nozzle geometry on the methane direct injection process in internal combustion engines," in *WCX SAE World Congress Experience* (SAE International, 2022).

[88]P. J. Roache, *Quantification of Uncertainty in Computational Fluid Dynamics* (Annual Review of Fluid Mechanics, 1997).
[89]F. Duronio, S. Ranieri, A. Montanaro, L. Allocca, and A. De Vita, "ECN spray G injector: Numerical modelling of flash-boiling breakup and spray collapse," Int. J. Multiphase Flow **145**, 103817 (2021).
[90]A. Di Mascio, G. Dubbioso, and R. Muscari, "Vortex structures in the wake of a marine propeller operating close to a free surface," J. Fluid Mech. **949**, A33 (2022).
[91]S. B. Pope and S. B. Pope, *Turbulent Flows* (Cambridge University Press, 2000).
[92]S. Jahangir, E. C. Wagner, R. F. Mudde, and C. Poelma, "Void fraction measurements in partial cavitation regimes by x-ray computed tomography," Int. J. Multiphase Flow **120**, 103085 (2019).
[93]D. Bauer, F. Barthel, and U. Hampel, "High-speed x-ray CT imaging of a strongly cavitating nozzle flow," J. Phys. Commun. **2**, 075009 (2018).
[94]C. E. Reagents, see https://www.carloerbareagents.com/cerstorefront/cer-exp/c/Sodium-hydroxide\%2C-pellets\%2C-98\%25/p/A16037 for "Sodium hydroxide, pellets, 98%" (last accessed April 2, 2023).
[95]J. Ozonek, *Application of Hydrodynamic Cavitation in Environmental Engineering* (CRC Press, 2012).
[96]S. K. Pawar, A. V. Mahulkar, A. B. Pandit, K. Roy, and V. S. Moholkar, "Sonochemical effect induced by hydrodynamic cavitation: Comparison of venturi/orifice flow geometries," AIChE J. **63**, 4705–4716 (2017).
[97]P. H. L. Alves, P. de, S. L. Silva, D. C. Ferreira, and J. C. de S. I. Gonçalves, "COD removal from sucrose solution using hydrodynamic cavitation and hydrogen peroxide: A comparison between Venturi device and orifice plate," Rev. Bras. Recur. Hidricos **24**, e12 (2019).
[98]A. Mukherjee, A. Mullick, R. Teja, P. Vadthya, A. Roy, and S. Moulik, "Performance and energetic analysis of hydrodynamic cavitation and potential integration with existing advanced oxidation processes: A case study for real life greywater treatment," Ultrason. Sonochem. **66**, 105116 (2020).
[99]P. S. Kumar, M. S. Kumar, and A. Pandit, "Experimental quantification of chemical effects of hydrodynamic cavitation," Chem. Eng. Sci. **55**, 1633–1639 (2000).